

---

# Monocular Depth Estimation using Diffusion Models

---

Saurabh Saxena<sup>1</sup> Abhishek Kar<sup>1</sup> Mohammad Norouzi<sup>1</sup> David J. Fleet<sup>1</sup>

## Abstract

We formulate monocular depth estimation using denoising diffusion models, inspired by their recent successes in high fidelity image generation. To that end, we introduce innovations to address problems arising due to noisy, incomplete depth maps in training data, including *step-unrolled denoising diffusion*, an  $L_1$  loss, and depth infilling during training. To cope with the limited availability of data for supervised training, we leverage pre-training on self-supervised image-to-image translation tasks. Despite the simplicity of the approach, with a generic loss and architecture, our *DepthGen* model achieves SOTA performance on the indoor NYU dataset, and near SOTA results on the outdoor KITTI dataset. Further, with a multimodal posterior, DepthGen naturally represents depth ambiguity (e.g., from transparent surfaces), and its zero-shot performance combined with depth imputation, enable a simple but effective text-to-3D pipeline. Project page: <https://depth-gen.github.io>

## 1. Introduction

Diffusion probabilistic models have emerged as a powerful family of generative models for high fidelity image synthesis, capturing remarkably rich knowledge about the visual world (Sohl-Dickstein et al., 2015; Ho et al., 2020; Ramesh et al., 2022; Saharia et al., 2022b). Given their impressive generative capabilities, it is natural to ask to what extent are these models effective for image to image vision tasks like segmentation, optical flow or depth estimation? Here, we adapt diffusion models to the problem of monocular depth estimation and investigate their effectiveness in the context of a large body of prior work. We demonstrate state of the art performance on benchmarks while also enabling multi-modal inference to resolve depth ambiguities, and exploiting depth imputation for text to 3D generation.

Two key issues in training diffusion models for monocular depth inference concern the amount and quality of available training data. First, much of the existing data is noisy

and incomplete (e.g., see Figs. 3 and 9). This presents a challenge for the conventional training framework and iterative sampling in diffusion models, leading to a problematic distribution shift between training and testing. To mitigate these issues we propose the use of an  $L_1$  loss for robustness, infilling missing depth values during training, and the introduction of *step-unrolled denoising diffusion*.

Given the limited availability of labelled training data, we also consider the use of self-supervised pre-training. This leverages the strong performance of diffusion models on tasks like colorization and inpainting (e.g., Saharia et al., 2022a), capturing rich image structure that may transfer to other tasks. Accordingly, we propose a training pipeline comprising multi-task self-supervised pre-training followed by supervised fine-tuning. The model can then be used zero-shot or it can be further fine-tuned for a specific domain.

The resulting model, *DepthGen*, outperforms SOTA baselines on the indoor NYU dataset, and is competitive on KITTI. Ablations show that unsupervised pre-training, depth infilling, the  $L_1$  loss, and step-unrolled denoising diffusion all significantly improve performance. As a probabilistic model, DepthGen has other attractive properties: With its ability to represent multi-modal distributions, we find that it can resolve depth ambiguities, e.g., due to reflective or transparent surfaces. Given the ease of imputation with diffusion models, DepthGen can also be used to infer missing depth values. We exploit this property, along with its zero-shot capability and existing text to image models to build a simple but effective framework for text to 3D scene generation and novel view synthesis.

In summary, our contributions are as follows:

1. We introduce DepthGen, a diffusion model for monocular depth estimation, comprising self-supervised pre-training and supervised fine-tuning. Without specialized loss functions or architectures, it achieves SOTA relative error of 0.074 on the NYU benchmark.
2. To train diffusion models on noisy, incomplete depth data, we advocate the use of an  $L_1$  loss, depth infilling, and step-unrolled denoising diffusion (SUD) to reduce latent distribution shift between training and inference.
3. We show that DepthGen enables multimodal depth inference, and imputation of missing depths e.g, for text-to-3D generation and novel view synthesis.

---

<sup>1</sup>Google Research. Correspondence to: Saurabh Saxena <srbs@google.com>.

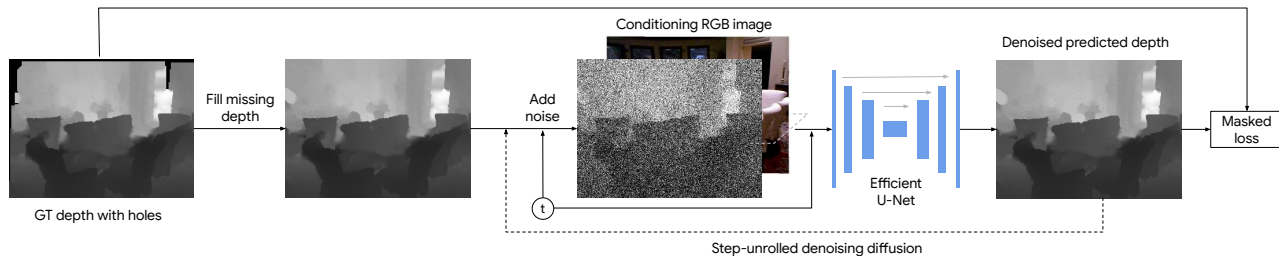


Figure 1. Training Architecture. Given a groundtruth depth map, we first infill missing depth using nearest neighbor interpolation. Then, following standard diffusion training, we add noise to the depth map and train a neural network to predict the noise given the RGB image and noisy depth map. During finetuning, we unroll one step of the forward pass and replace the groundtruth depth map with the prediction.

## 2. Related Work

**Monocular depth estimation** is essential for many vision applications (Jing et al., 2022; Zhou et al., 2019). And recent progress has been impressive, with the development of specialized loss functions and architectures (e.g., Saxena et al., 2005; 2009; Eigen et al., 2014; Eigen & Fergus, 2014; Laina et al., 2016; Cao et al., 2016; Fu et al., 2018; Bhat et al., 2021; Li et al., 2022; Agarwal & Arora, 2022). We build on this rich literature, but with a simple, generic architecture, leveraging recent advances in generative models.

Prior work has shown that self-supervised tasks like colorization (Zhang et al., 2016; Larsson et al., 2016) serve as effective pre-training for downstream vision tasks. This motivates the choice to initialize our model with Palette (Saharia et al., 2022a) style multi-task pre-training on the self-supervised image-to-image translation tasks. Self-supervised training using masked prediction has also recently been found to be particularly effective (Xie et al., 2022), with subsequent work, concurrent to ours, establishing the current SOTA (Ning et al., 2023). Our findings also support self-supervised pre-training, albeit with diffusion-based image-to-image translation, and we establish a new SOTA while also representing multi-modality and supporting zero-shot depth completion.

Large-scale in-domain pre-training has also been effective for depth estimation (Ranftl et al., 2019; 2021; Ren & Lee, 2017), which we find to be the case here as well.

**Diffusion models** have excelled at image generation, including unconditional and class-conditional generation (Dhariwal & Nichol, 2022; Ho et al., 2022a), image-to-image translation (Saharia et al., 2022c;a), text-to-image synthesis (Rombach et al., 2022; Ramesh et al., 2022; Nichol et al., 2021; Saharia et al., 2022b), and text-guided image editing (Brooks et al., 2022; Wang et al., 2022; Hertz et al., 2022; Meng et al., 2021). Despite this success, they have not been widely applied to vision tasks, except for recent work on image enhancement (Saharia et al., 2022a), used here for pre-training, and work on panoptic segmentation (Chen et al., 2022). To the best of our knowledge, ours is the first to apply diffusion models to monocular depth estimation.

Also related to our work are diffusion models for view synthesis from multi-view image data (Watson et al., 2022), generative models for point cloud data (Nichol et al., 2022), text-to-3D generative models (Poole et al., 2022) and models for depth-aware novel view synthesis (Rockwell et al., 2021; Liu et al., 2021). While work on 3D generative models is exciting, our primary interest here is monocular depth estimation.

## 3. DepthGen

### 3.1. Background

Diffusion models are latent-variable generative models trained to transform a sample of a Gaussian noise into a sample from a data distribution (Sohl-Dickstein et al., 2015; Ho et al., 2020). They comprise a *forward process* that gradually annihilates data by adding noise, as ‘time’  $t$  increases from 0 to 1, and a learned *generative process* that reverses the forward process, starting from a sample of random noise at  $t = 1$  and incrementally adding structure (attenuating noise) as  $t$  decreases to 0. A conditional diffusion model conditions the steps of the reverse process. In the case of depth estimation, our conditioning signal is an RGB image,  $\mathbf{x}$ , and the target is a conditional distribution over depth maps,  $p(\mathbf{y} | \mathbf{x})$ .

Central to the model is a denoising network  $f_\theta$  that is trained to take a noisy sample at some time-step  $t$ , and predict a less noisy sample. Using Gaussian noise in the forward process, one can express the training objective over the sequence of transitions (as  $t$  slowly decreases) as a sum of non-linear regression losses, i.e.,

$$\mathbb{E}_{(\mathbf{x}, \mathbf{y})} \mathbb{E}_{(t, \epsilon)} \left\| f_\theta(\mathbf{x}, \underbrace{\sqrt{\gamma_t} \mathbf{y} + \sqrt{1-\gamma_t} \epsilon}_{\mathbf{y}_t}, t) - \epsilon \right\|_2^2 \quad (1)$$

where  $\epsilon \sim \mathcal{N}(0, I)$ ,  $t \sim \mathcal{U}(0, 1)$ , and where  $\gamma_t > 0$  is computed with a pre-determined noise schedule. For inference (i.e., sampling), one draws a random noise sample  $\mathbf{y}_1$ , and then iteratively uses  $f_\theta$  to estimate the noise, from which one can compute the next latent sample  $\mathbf{y}_s$ , for  $s < t$ .

### 3.2. Self-Supervised Pre-Training

DepthGen training comprises self-supervised pre-training, then supervised training on RGB-D data. The pre-trained model is a self-supervised multi-task diffusion model. Following (Saharia et al., 2022a), we train a Palette model from scratch on four image-to-image translation tasks, i.e., colorization, inpainting, uncropping and JPEG artifact removal.

### 3.3. Supervised training with noisy, incomplete depth

Following pre-training, and with minor modifications to the architecture (see Sec. 4.2), training continues on paired RGB and depth data. While straightforward conceptually, the training datasets available for depth estimation present substantial challenges. The depth maps in particular are noisy and often contain regions with missing depth values. The various causes for such *holes* are due to highly reflective surfaces, light absorbing surfaces (Stommel et al., 2014) or regions outside the sensor’s range of measurement. Holes are largely inconsequential for simple feed-forward nets or regression models, since one could only backpropagate the loss from the subset of pixels with known depth values, ignoring those with missing depth. For diffusion models, however, such corruption of the training data is problematic.

Diffusion models perform inference through iterative refinement – in our case, of a depth map  $y$  conditioned on an RGB image  $x$ . It starts with a sample of Gaussian noise  $y_1$ , and terminates with a sample from the predictive distribution  $p(y_0 | x)$ . A refinement step from time  $t$  to  $s$ , with  $s < t$ , proceeds by sampling from the parameterized distribution  $p_\theta(y_s | y_t, x)$ . Simply put, during inference, each step operates on the output from the previous step. In contrast, at training the different steps are somewhat decoupled (see Eqn. 1), where the denoising network operates on a noisy version of the ground truth depth map instead of the output of the previous iteration (reminiscent of teaching forcing in training RNNs). This introduces a distribution shift between training and inference, since the marginal distribution over noisy training depth maps *with holes* may differ significantly from the distribution of noisy depths at inference time, which should ideally (since we do not learn the distribution of holes in the loss) be a noisy version of the *true*, complete depth maps (from a perfect, noiseless sensor for instance). This has a significant negative impact on model performance. This problem is further exacerbated by structured or heavy-tailed noise in training depth maps.

We find that these problems are effectively mitigated with the following modifications during training:

**Depth interpolation.** To reduce distribution shift between training and inference we impute missing depth values. We explored several ways to accomplish this, including various interpolation schemes, and using DepthGen (trained with

---

#### Algorithm 1 Train step w/ infilling and SUD.

---

```

Input: rgb image  $x$ , depth map  $y$ 
 $t \leftarrow U(0, 1)$ 
 $\epsilon \leftarrow N(0, 1)$ 
 $valid\_mask = y > 0$ 
 $y = fill\_holes(y)$ 
 $y_t = \sqrt{\gamma_t} * y + \sqrt{1 - \gamma_t} * \epsilon$ 
if  $unroll\_step$  then
     $\epsilon_{pred} = stop\_grad(f_\theta(x, y_t, t))$ 
     $y_{pred} = (y_t - \sqrt{1 - \gamma_t} * \epsilon_{pred}) / \sqrt{\gamma_t}$ 
     $y_t = \sqrt{\gamma_t} * y_{pred} + \sqrt{1 - \gamma_t} * \epsilon$ 
     $\epsilon = (y_t - \sqrt{\gamma_t} * y) / \sqrt{1 - \gamma_t}$ 
end if
 $\epsilon_{pred} = f_\theta(x, y_t, t)$ 
 $loss = reduce\_mean(|\epsilon - \epsilon_{pred}|[valid\_mask])$ 
    
```

---

nearest neighbor interpolation infilling) to infill missing depth. But, empirically, we found that two straightforward steps performed as well as more sophisticated approaches. In particular, we find that nearest neighbor interpolation is sufficient to impute missing depths in indoor training data. For outdoor data we continue to use nearest neighbor interpolation, except for sky regions, as they are often large and are much further from the camera than adjacent objects in the image. We use an off-the-shelf sky segmenter (Liba et al., 2020), and then set all sky pixels to be the maximum modeled depth (here, 80m). Despite the imputation of missing depths, we note that the training loss is only computed at pixels with known (vs infilled) depth.

**Step-unrolled Denoising Diffusion.** Another approach to tackling the distribution shift in the latent marginal distribution of  $y_t$  between training and inference is to construct  $y_t$  using the model’s output instead of the ground truth depth. One can do this by slightly modifying the training procedure (Algorithm 1) to run one forward pass of the model and build  $y_t$  by adding noise to the model’s output rather than the training depth map. We do not propagate gradients for this forward pass. We find that this slows down training by about 15% on a TPU v4. We refer to this as *step-unrolled denoising diffusion (SUD)*.

We perform SUD during fine-tuning only, not during supervised depth pre-training. Early in training the depth predictions are likely inaccurate. So the latent marginals over the noisy training depth maps would be much closer to the desired *true* marginals than those produced by adding noise to the model’s outputs. Hence, doing SUD early in supervised pre-training is not recommended. One might consider the use of a curriculum for gradually introducing SUD in the later stages of supervised pre-training, but this also introduces additional hyper-parameters, so we simply invoke SUD during fine-tuning, and leave an exploration of curricula to future work.

This problem of training / inference distribution shift resembles that of *exposure bias* (Ranzato et al., 2016) in autoregressive models, for which the mismatch is caused by *teacher forcing* during training (Williams & Zipser, 1989). Several solutions have been proposed for this problem in the literature (Lamb et al., 2016; Yu et al., 2016; Bengio et al., 2015). SUD also closely resembles the approach in (Savinov et al., 2022) where they perform step-unrolling for training denoising autoencoders on text.

Finally, we note that (Ning et al., 2023) faced a similar problem when training a vector-quantizer on depth data. They work around it by synthetically adding more holes following a carefully chosen masking ratio. In comparison, we prefer our approach since nearest neighbor infilling is hyperparameter free and step-unrolled denoising diffusion could be more generally applicable to other tasks with sparse data.

$L_1$  Loss. While the  $L_2$  loss in Eqn. 1 is appropriate for noise-free training data with additive Gaussian noise, good performance has been reported with an  $L_1$  loss during training for image-to-image translation models (Saharia et al., 2022c). Given the possibility of substantial noise in depth data, especially for large depths and near holes, we hypothesize that the robustness afforded by the  $L_1$  loss may also be useful in training RGB-to-depth diffusion models.

## 4. Experiments

### 4.1. Datasets

For unsupervised pre-training, we use the ImageNet-1K (Deng et al., 2009) and Places365 (Zhou et al., 2017) datasets and train on the self-supervised tasks of colorization, inpainting, uncropping, and JPEG decompression, following (Saharia et al., 2022a).

**Indoor model.** For supervised image-to-depth pre-training of the indoor model we use the following two datasets (with dataset mixing at the batch level):

*ScanNet* (Dai et al., 2017) is a dataset of 2.5M images captured using a Kinect v1-like sensor. It provides depth maps at  $640 \times 480$  and RGB images at  $1296 \times 968$ .

*SceneNet RGB-D* (McCormac et al., 2016) is a synthetic dataset of 5M images generated by rendering ShapeNet (Chang et al., 2015) objects in scenes from SceneNet (Handa et al., 2015) at a resolution of  $320 \times 240$ .

For indoor fine-tuning and evaluation we use *NYU depth v2* (Silberman et al., 2012), a commonly used dataset for evaluating indoor depth prediction models. It provides aligned image and depth maps at  $640 \times 480$  resolution. We use the official split consisting of 50k images for training and 654 images for evaluation. The predicted depth maps from our model are resized to the full resolution using bilinear

up-sampling before evaluation. We evaluate on a cropped region proposed by (Eigen et al., 2014) following prior work.

**Outdoor model.** For outdoor model training we use the *Waymo Open Dataset* (Sun et al., 2020), a large-scale driving dataset consisting of about 200k frames. Each frame provides RGB images from 5 cameras and LiDAR maps. We use the RGB images from the FRONT, FRONT\_LEFT and FRONT\_RIGHT cameras and the TOP LiDAR only to build about 600k aligned RGB depth maps.

For subsequent fine-tuning and evaluation, we use *KITTI* (Geiger et al., 2013), an outdoor driving dataset which provides RGB images and LiDAR scans at resolutions close to  $1226 \times 370$ . We use the training/test split proposed by (Eigen et al., 2014), comprising 26k training images and 652 test images. The predicted depth from DepthGen is up-sampled to the full resolution using bilinear interpolation before evaluation. We evaluate on a cropped region proposed in (Garg et al., 2016) following prior work.

**Data Augmentation and Preprocessing** We use random horizontal flip data augmentation for supervised depth training which is common in prior work. Where needed, images and depth maps are resized using bilinear interpolation to the model’s resolution for training. Diffusion models expect inputs and generate outputs in the range  $[-1., 1.]$ . For the indoor model we use a max depth of 10 meters, and for the outdoor model we normalize the depth maps to the range with a maximum depth of 80 meters.

### 4.2. Architecture

The predominant architecture for diffusion models is the U-Net developed for the DDPM model (Ho et al., 2020), and later improved in several respects (Nichol & Dhariwal, 2021; Song et al., 2021; Dhariwal & Nichol, 2022). For DepthGen, we adapt the *Efficient U-Net* architecture that was developed for Imagen (Saharia et al., 2022b). The Efficient U-Net architecture is more efficient than the U-Nets used in prior work, because it has fewer self-attention layers, fewer parameters and less computation at higher resolutions, along with other adjustments that make it well suited to training medium resolution diffusion models.

We make several minor changes to this architecture to adapt it for image-to-depth models. We drop the text cross-attention layers but keep the self-attention layer. Efficient U-Net has six input and three output channels, since the target is a RGB image (input consists of a 3-channel source RGB image and a 3-channel noisy target image concatenated along the channel dimension). For depth models, since we have a scalar output image, we modify the architecture to have four input channels and one output channel. Note that this means we need to reinitialize the input and output convolutional kernels before the supervised depth

Table 1. Comparison of performances on the NYU-Depth-v2 dataset.  $\top$  indicates methods that use unsupervised pretraining,  $\dagger$  indicates supervised pretraining and  $\ddagger$  indicates methods with supervised depth pretraining on auxiliary data. **Best** / second best / *third best* results are bolded / underlined / italicized respectively.  $\downarrow$  denotes lower is better and  $\uparrow$  denotes higher is better. Baselines: [1] Fu et al. (2018), [2] Yin et al. (2019), [3] Lee et al. (2019), [4] Huynh et al. (2020), [5] Zhao et al. (2021), [6] Ranftl et al. (2021), [7] Bhat et al. (2021), [8] Li et al. (2022), [9] Agarwal & Arora (2022), [10] Xie et al. (2022), [11] Ning et al. (2023). \* denotes concurrent work.

| Method          | Architecture                   | $\delta_1 \uparrow$ | $\delta_2 \uparrow$ | $\delta_3 \uparrow$ | REL $\downarrow$ | RMS $\downarrow$ | $\log_{10} \downarrow$ |
|-----------------|--------------------------------|---------------------|---------------------|---------------------|------------------|------------------|------------------------|
| DORN [1]        | ResNet-101 $\dagger$           | 0.828               | 0.965               | 0.992               | 0.115            | 0.509            | 0.051                  |
| VNL [2]         | ResNeXt-101 $\dagger$          | 0.875               | 0.976               | 0.994               | 0.108            | 0.416            | 0.048                  |
| BTS [3]         | DenseNet-161 $\dagger$         | 0.885               | 0.978               | 0.994               | 0.110            | 0.392            | 0.047                  |
| DAV [4]         | DRN-D-22 $\dagger$             | 0.882               | 0.980               | 0.996               | 0.108            | 0.412            | –                      |
| TransDepth [5]  | Res-50+ViT-B $\dagger$         | 0.900               | 0.983               | 0.996               | 0.106            | 0.365            | 0.045                  |
| DPT [6]         | Res-50+ViT-B $\ddagger$        | 0.904               | 0.988               | <u>0.998</u>        | 0.110            | 0.357            | 0.045                  |
| AdaBins [7]     | E-B5+Mini-ViT $\dagger$        | 0.903               | 0.984               | <i>0.997</i>        | 0.103            | 0.364            | 0.044                  |
| BinsFormer [8]  | Swin-Large $\dagger$           | 0.925               | 0.989               | <i>0.997</i>        | 0.094            | 0.330            | 0.040                  |
| PixelFormer [9] | Swin-Large $\dagger$           | 0.929               | <i>0.991</i>        | <u>0.998</u>        | 0.090            | 0.322            | 0.039                  |
| MIM [10]        | SwinV2-L $\top$                | <u>0.949</u>        | <b>0.994</b>        | <b>0.999</b>        | 0.083            | <u>0.287</u>     | <i>0.035</i>           |
| AiT-P [11]*     | SwinV2-L $\top$                | <b>0.953</b>        | <u>0.993</u>        | <b>0.999</b>        | <i>0.076</i>     | <b>0.279</b>     | <u>0.033</u>           |
| DepthGen (ours) |                                |                     |                     |                     |                  |                  |                        |
| samples=1       | Efficient U-Net $\top\ddagger$ | 0.944               | 0.986               | 0.995               | <u>0.075</u>     | 0.324            | <b>0.032</b>           |
| samples=2       | Efficient U-Net $\top\ddagger$ | 0.944               | 0.987               | 0.996               | <b>0.074</b>     | 0.319            | <b>0.032</b>           |
| samples=4       | Efficient U-Net $\top\ddagger$ | <i>0.946</i>        | 0.987               | 0.996               | <b>0.074</b>     | 0.315            | <b>0.032</b>           |
| samples=8       | Efficient U-Net $\top\ddagger$ | <i>0.946</i>        | 0.987               | 0.996               | <b>0.074</b>     | <i>0.314</i>     | <b>0.032</b>           |

pretraining stage.

**Resolution.** Our re-trained Palette model was trained for images at a resolution of  $256 \times 256$ . For training depth models we choose resolutions that are close to this while preserving the aspect ratios of the original depth training datasets. The indoor model is trained at  $320 \times 240$ . For Waymo we use  $384 \times 256$  and for KITTI  $416 \times 128$ . The model does not contain learned positional embeddings so it can be easily pretrained and finetuned at different resolutions.

### 4.3. Hyper-parameters

The self-supervised model is trained for 2.8M steps with an  $L_2$  loss and a mini-batch size of 512. Other hyper-parameters are similar to those in the original Palette paper.

The depth models are trained with  $L_1$  loss. We use a constant learning rate of  $1e-4$  during supervised depth pretraining but switch to a slightly lower learning rate of  $3e-5$  during fine-tuning which we find achieves slightly better results. We do learning rate warm-up over 10k steps for all models. All depth models are trained with a smaller mini-batch size of 64. The indoor depth model is trained on a mix of ScanNet and SceneNet RGBD for 2M steps and then fine-tuned on NYU for 50k steps. The outdoor depth model is trained on Waymo for 0.9M steps and fine-tuned on KITTI for 50k steps. Other details, like the optimizer and the use of EMA are similar to those outlined in (Saharia et al., 2022a).

### 4.4. Sampler

We use the DDPM ancestral sampler (Ho et al., 2020) with 128 denoising steps. Increasing the number of denoising steps further did not greatly improve performance. We have not yet explored progressive distillation (Salimans & Ho, 2022) for faster sampling. We believe the results on distillation for generative image models should transfer well to image-to-depth models, thereby, reducing the gap between the speed of diffusion sampling and single-step depth estimation models. We leave this exploration to future work.

### 4.5. Evaluation metrics

We follow the standard evaluation protocol used in prior work (Li et al., 2022). For both the NYU depth v2 and KITTI datasets we report the absolute relative error (REL), root mean squared error (RMS) and accuracy metrics ( $\delta_i < 1.25^i$  for  $i \in 1, 2, 3$ ). For NYU we additionally report absolute error of log depths ( $\log_{10}$ ). For KITTI we additionally report the squared relative error (Sq-rel) and root mean squared error of log depths (RMS log).

### 4.6. Results

Table 1 shows the results on NYU depth v2. We achieve a state-of-the-art absolute relative error of 0.074. Table 2 shows results on KITTI, where we perform competitively with prior work. We report results with averaging depth maps from one or more samples. Note that most prior

Table 2. Comparison of performances on the KITTI dataset.  $\top$  indicates methods that use unsupervised pretraining,  $\dagger$  indicates supervised pretraining, and  $\ddagger$  indicates methods with supervised depth pretraining on auxiliary data. **Best** / second best / *third best* results are bolded / underlined / italicized respectively.  $\downarrow$  denotes lower is better and  $\uparrow$  denotes higher is better. E-B5: EfficientNet-B5 (Tan & Le, 2019). Baselines: [11] (Godard et al., 2017), [12] (Johnston & Carneiro, 2020), [13] (Gan et al., 2018), [1] Fu et al. (2018), [2] Yin et al. (2019), [14] (Xu et al., 2020), [3] Lee et al. (2019), [5] Zhao et al. (2021), [6] Ranftl et al. (2021), [7] Bhat et al. (2021), [8] Li et al. (2022), [9] Agarwal & Arora (2022), [10] Xie et al. (2022).

| Method               | Backbone                       | $\delta_1 \uparrow$ | $\delta_2 \uparrow$ | $\delta_3 \uparrow$ | REL $\downarrow$ | Sq-rel $\downarrow$ | RMS $\downarrow$ | RMS log $\downarrow$ |
|----------------------|--------------------------------|---------------------|---------------------|---------------------|------------------|---------------------|------------------|----------------------|
| Godard et al. [11]   | ResNet-50                      | 0.861               | 0.949               | 0.976               | 0.114            | 0.898               | 4.935            | 0.206                |
| Johnston et al. [12] | ResNet-101 $\dagger$           | 0.889               | 0.962               | 0.982               | 0.106            | 0.861               | 4.699            | 0.185                |
| Gan et al. [13]      | ResNet-101                     | 0.890               | 0.964               | 0.985               | 0.098            | 0.666               | 3.933            | 0.173                |
| DORN [1]             | ResNet-101 $\dagger$           | 0.932               | 0.984               | 0.994               | 0.072            | 0.307               | 2.727            | 0.120                |
| VNL [2]              | ResNext-101 $\dagger$          | 0.938               | 0.990               | <i>0.998</i>        | 0.072            | –                   | 3.258            | 0.117                |
| PGA-Net [14]         | ResNet-50 $\ddagger$           | 0.952               | 0.992               | <i>0.998</i>        | 0.063            | 0.267               | 2.634            | 0.101                |
| BTS [3]              | DenseNet-161 $\dagger$         | 0.956               | 0.993               | <i>0.998</i>        | 0.059            | 0.245               | 2.756            | 0.096                |
| TransDepth [5]       | ResNet-50+ViT-B $\dagger$      | 0.956               | 0.994               | <u>0.999</u>        | 0.064            | 0.252               | 2.755            | 0.098                |
| DPT [6]              | ResNet-50+ViT-B $\ddagger$     | 0.959               | <i>0.995</i>        | <u>0.999</u>        | 0.062            | –                   | 2.573            | 0.092                |
| AdaBins [7]          | E-B5+mini-ViT $\dagger$        | 0.964               | <i>0.995</i>        | <u>0.999</u>        | 0.058            | 0.190               | 2.360            | 0.088                |
| BinsFormer [8]       | Swin-Large $\dagger$           | <i>0.974</i>        | <u>0.997</u>        | <u>0.999</u>        | <i>0.052</i>     | <i>0.151</i>        | <u>2.098</u>     | <i>0.079</i>         |
| PixelFormer [9]      | Swin-Large $\dagger$           | <u>0.976</u>        | <u>0.997</u>        | <u>0.999</u>        | <u>0.051</u>     | <u>0.149</u>        | <u>2.081</u>     | <u>0.077</u>         |
| MIM [10]             | SwinV2-L $\top$                | <b>0.977</b>        | <b>0.998</b>        | <b>1.000</b>        | <b>0.050</b>     | <b>0.139</b>        | <b>1.966</b>     | <b>0.075</b>         |
| DepthGen (ours)      |                                |                     |                     |                     |                  |                     |                  |                      |
| samples=1            | Efficient U-Net $\top\ddagger$ | 0.951               | 0.991               | 0.997               | 0.064            | 0.389               | 3.104            | 0.103                |
| samples=2            | Efficient U-Net $\top\ddagger$ | 0.951               | 0.991               | <i>0.998</i>        | 0.064            | 0.378               | 3.07             | 0.102                |
| samples=4            | Efficient U-Net $\top\ddagger$ | 0.951               | 0.991               | <i>0.998</i>        | 0.064            | 0.373               | 3.052            | 0.102                |
| samples=8            | Efficient U-Net $\top\ddagger$ | 0.953               | 0.991               | <i>0.998</i>        | 0.064            | 0.356               | 2.985            | 0.100                |

Table 3. Ablations for pre-training (before fine-tuning), showing absolute relative error with a single sample for NYU and KITTI.

|  | NYU $\downarrow$ | KITTI $\downarrow$ |
|--|------------------|--------------------|
| Training from scratch                  | 0.155            | 0.103              |
| Self-supervised pre-training only      | 0.116            | 0.086              |
| Supervised pre-training only           | 0.081            | 0.075              |
| Self-supervised & supervised pre-train | 0.075            | 0.064              |

Table 4. Ablation for handling incomplete depth showing absolute relative error with a single sample on NYU and KITTI.

|                   | NYU $\downarrow$ | KITTI $\downarrow$ |
|-------------------|------------------|--------------------|
| Baseline          | 0.079            | 0.115              |
| SUD only          | 0.076            | 0.075              |
| Infilling only    | 0.077            | 0.066              |
| SUD and infilling | 0.075            | 0.064              |

works report average over two samples obtained by left-right reflection of the input image.

#### 4.7. Ablations

We find that both pre-training and accounting for missing depth are crucial to model performance. Table 3 shows that both self-supervised pre-training and supervised depth pre-training are important, with supervised depth training having a larger impact, which is to be expected. Table 4 shows that depth infilling is extremely important for the outdoor KITTI dataset. It has less impact on NYU, which

Table 5. Ablation for  $L_1$  vs  $L_2$  loss showing absolute relative error with a single sample on NYU and KITTI.

|       | NYU $\downarrow$ | KITTI $\downarrow$ |
|-------|------------------|--------------------|
| $L_2$ | 0.085            | 0.071              |
| $L_1$ | 0.075            | 0.064              |

is understandable since KITTI has sparser depth maps. In the absence of filled depth maps, step-unrolled denoising diffusion dramatically improves results especially on KITTI. Even with depth infilling, SUD consistently improves performance for both indoor and outdoor datasets. Additionally, we ablate the choice of loss function in Table 5. We find that the  $L_1$  loss yields better performance than  $L_2$ , likely because  $L_1$  is more robust to noise at larger depths. (See Appendix for metrics other than absolute relative error.)

#### 4.8. Multimodality

One strength of diffusion models is their ability to capture complex multimodal distributions. This can be effective in representing depth uncertainty, especially where there may exist natural depth ambiguities, e.g., in cases of transparency when looking through a window. Figures 2 and 3 present multiple samples on the NYU and KITTI datasets which show that the model captures multimodality in sensor data and provides plausible samples in case of ambiguities.

## Monocular Depth Estimation using Diffusion Models

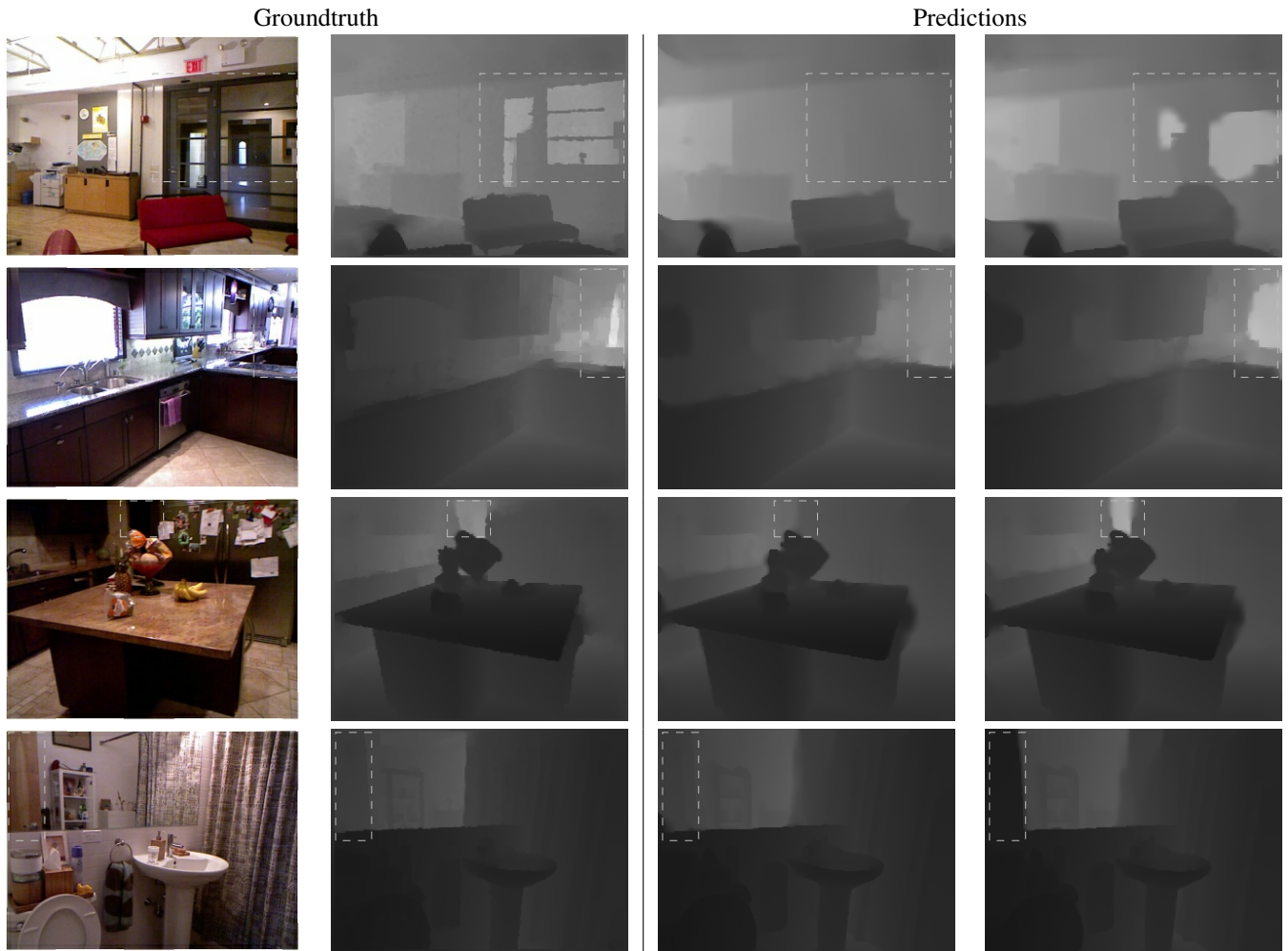


Figure 2. Examples of multimodal predictions on the NYU Depth V2 val dataset. Rows 1-2 contain glass doors/windows where the model learns to predict the depth for either the glass surface or the surface behind it. Row 3 has a dark area next to the refrigerator for which the depth is unclear from RGB alone. In row 4 the model hallucinates the reflected door as a bath cabinet, which seems plausible from the RGB image.



Figure 3. Multimodal depth predictions on the KITTI val dataset.



Prompt: A bedroom.



Prompt: A living room.

Figure 4. Text to 3D samples. Given a text prompt, an image is first generated using Imagen (first row of first column), after which depth is estimated (second row of first column). Subsequently the camera is moved to reveal new parts of the scene, which are then infilled using an image completion model and DepthGen (which conditions on both the incomplete depth map and the filled image). At each step, newly generated RGBD points are added to a global point cloud which is visualized in the rightmost column. See 6 for more samples.

#### 4.9. Novel View Synthesis

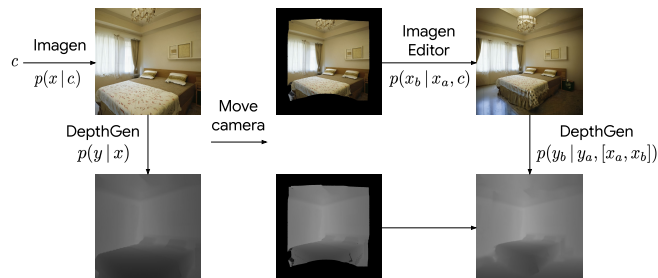


Figure 5. Pipeline for iteratively generating a 3D scene conditioned on text  $c = A\ bedroom$ . See text for details.

One advantage of diffusion models is the ease with which one can zero-shot impute one part of an image (or depth map) conditioned on the rest of the image (or depth map). Here, we leverage this to build a limited but effective text-to-3D scene generation pipeline. As depicted in Figure 5, we use the Imagen text-to-image model to generate an image, given text  $c$ , to which we apply DepthGen (zero-shot) to sample a corresponding depth map. We then move the camera and, following (Liu et al., 2021), render the RGBD point cloud from a new camera pose. Of course this only provides RGB and depth values at a subset of pixels in the new frame since the fields of view are different. Fortunately, the missing pixels are easily inferred using diffusion models (i.e., the Imagen Editor (Wang et al., 2022) and DepthGen).

Let  $x_a$  and  $y_a$  be the RGB and depth values at pixel loca-

tions rendered from the new camera pose respectively, and let  $x_b$  and  $y_b$  correspond to lines of sight not visible in the original frame. We first infer the missing RGB values, i.e.,  $p(x_b|x_a, c)$ , using the uncropping/inpainting capability of the Imagen Editor. We then use DepthGen to impute the missing depth values, i.e., sampling from  $p(y_b|y_a, [x_a, x_b])$ . There are several effective solutions to imputation with diffusion models, including the replacement method in (Song et al., 2021), and the more sophisticated use of reconstruction guidance in (Ho et al., 2022b). For simplicity we use the replacement method to sample the unknown depths  $y_b$  conditioned on existing depths  $y_a$  and the image  $x = [x_a, x_b]$ .

## 5. Conclusion

We propose a novel approach to monocular depth estimation using denoising diffusion models. We leverage self-supervised image-to-image pre-training, followed by subsequent training on supervised depth data to achieve SOTA results on challenging depth estimation benchmarks. We make several innovations that make it possible to effectively train diffusion models on imperfect training data that are commonplace for depth estimation. We demonstrate the multimodal capability of diffusion models to represent depth uncertainty. And we exploit the ease of imputation during iterative refinement in diffusion models to show how DepthGen can be used for zero-shot depth completion. In combination with text-to-image diffusion models, this enables a simple pipeline for novel view synthesis and text-to-3D.

## References

- Agarwal, A. and Arora, C. Attention attention everywhere: Monocular depth prediction with skip attention. *arxiv:2210.09071*, 2022.
- Bengio, S., Vinyals, O., Jaitly, N., and Shazeer, N. Scheduled sampling for sequence prediction with recurrent neural networks. In *Proceedings of the 28th International Conference on Neural Information Processing Systems - Volume 1*, NIPS'15, pp. 1171–1179, Cambridge, MA, USA, 2015. MIT Press.
- Bhat, S. F., Alhashim, I., and Wonka, P. Adabins: Depth estimation using adaptive bins. In *Computer Vision and Pattern Recognition (CVPR)*, pp. 4009–4018, 2021.
- Brooks, T., Holynski, A., and Efros, A. A. Instruct-pix2pix: Learning to follow image editing instructions. *arXiv:2211.09800*, 2022.
- Cao, Y., Wu, Z., and Shen, C. Estimating depth from monocular images as classification using deep fully convolutional residual networks. *arXiv:1605.02305*, 2016.
- Chang, A. X., Funkhouser, T., Guibas, L., Hanrahan, P., Huang, Q., Li, Z., Savarese, S., Savva, M., Song, S., Su, H., Xiao, J., Yi, L., and Yu, F. ShapeNet: An information-rich 3d model repository. *arXiv:1512.03012*, 2015.
- Chen, T., Li, L., Saxena, S., Hinton, G., and Fleet, D. J. A generalist framework for panoptic segmentation of images and videos. *arXiv:2210.06366*, 2022.
- Dai, A., Chang, A. X., Savva, M., Halber, M., Funkhouser, T., and Nießner, M. ScanNet: Richly-annotated 3d reconstructions of indoor scenes. *arxiv:1702.04405*, 2017.
- Deng, J., Dong, W., Socher, R., Li, L.-J., Li, K., and Fei-Fei, L. ImageNet: A Large-Scale Hierarchical Image Database. In *CVPR09*, 2009.
- Dhariwal, P. and Nichol, A. Diffusion models beat GANs on image synthesis. In *NeurIPS*, 2022.
- Eigen, D. and Fergus, R. Predicting depth, surface normals and semantic labels with a common multi-scale convolutional architecture. *arXiv:1411.4734*, 2014.
- Eigen, D., Puhrsch, C., and Fergus, R. Depth map prediction from a single image using a multi-scale deep network. In *Advances in Neural Information Processing Systems (NIPS)*, volume 27, 2014.
- Fu, H., Gong, M., Wang, C., Batmanghelich, K., and Tao, D. Deep ordinal regression network for monocular depth estimation. In *Computer Vision and Pattern Recognition (CVPR)*, pp. 2002–2011, 2018.
- Gan, Y., Xu, X., Sun, W., and Lin, L. Monocular depth estimation with affinity, vertical pooling, and label enhancement. In *European Conference on Computer Vision (ECCV)*, pp. 224–239, 2018.
- Garg, R., Bg, V. K., Carneiro, G., and Reid, I. Unsupervised cnn for single view depth estimation: Geometry to the rescue. In *European Conference on Computer Vision (ECCV)*, pp. 740–756, 2016.
- Geiger, A., Lenz, P., Stiller, C., and Urtasun, R. Vision meets robotics: The kitti dataset. *The International Journal of Robotics Research*, 32(11):1231–1237, 2013.
- Godard, C., Mac Aodha, O., and Brostow, G. J. Unsupervised monocular depth estimation with left-right consistency. In *Computer Vision and Pattern Recognition (CVPR)*, pp. 270–279, 2017.
- Handa, A., Patraucean, V., Badrinarayanan, V., Stent, S., and Cipolla, R. Scenenet: Understanding real world indoor scenes with synthetic data. *arXiv:1511.07041*, 2015.
- Hertz, A., Mokady, R., Tenenbaum, J., Aberman, K., Pritch, Y., and Cohen-Or, D. Prompt-to-prompt image editing with cross attention control. *arXiv:2208.01626*, 2022.
- Ho, J., Jain, A., and Abbeel, P. Denoising Diffusion Probabilistic Models. *NeurIPS*, 2020.
- Ho, J., Saharia, C., Chan, W., Fleet, D. J., Norouzi, M., and Salimans, T. Cascaded diffusion models for high fidelity image generation. *Journal of Machine Learning Research*, 2022a.
- Ho, J., Salimans, T., Gritsenko, A., Chan, W., Norouzi, M., and Fleet, D. J. Video Diffusion Models. In *NeurIPS*, 2022b.
- Huynh, L., Nguyen-Ha, P., Matas, J., Rahtu, E., and Heikkilä, J. Guiding monocular depth estimation using depth-attention volume. In *European Conference on Computer Vision (ECCV)*, pp. 581–597. Springer, 2020.
- Jing, L., Yu, R., Kretzschmar, H., Li, K., Qi, C. R., Zhao, H., Ayvaci, A., Chen, X., Cower, D., Li, Y., You, Y., Deng, H., Li, C., and Anguelov, D. Depth estimation matters most: Improving per-object depth estimation for monocular 3d detection and tracking. *arXiv:2206.03666*, 2022.
- Johnston, A. and Carneiro, G. Self-supervised monocular trained depth estimation using self-attention and discrete disparity volume. In *Computer Vision and Pattern Recognition (CVPR)*, pp. 4756–4765, 2020.
- Laina, I., Rupprecht, C., Belagiannis, V., Tombari, F., and Navab, N. Deeper depth prediction with fully convolutional residual networks. In *2016 Fourth international conference on 3D vision (3DV)*, pp. 239–248, 2016.

- Lamb, A., Goyal, A., Zhang, Y., Zhang, S., Courville, A., and Bengio, Y. Professor forcing: A new algorithm for training recurrent networks. *arXiv:1610.09038*, 2016.
- Larsson, G., Maire, M., and Shakhnarovich, G. Learning representations for automatic colorization. *arXiv:1603.06668*, 2016.
- Lee, J. H., Han, M.-K., Ko, D. W., and Suh, I. H. From big to small: Multi-scale local planar guidance for monocular depth estimation. *arXiv:1907.10326*, 2019.
- Li, Z., Wang, X., Liu, X., and Jiang, J. Binsformer: Revisiting adaptive bins for monocular depth estimation. *arxiv.2204.00987*, 2022.
- Liba, O., Cai, L., Tsai, Y.-T., Eban, E., Movshovitz-Attias, Y., Pritch, Y., Chen, H., and Barron, J. T. Sky optimization: Semantically aware image processing of skies in low-light photography. In *Proceedings of the IEEE/CVF Conference on Computer Vision and Pattern Recognition (CVPR) Workshops*, June 2020.
- Liu, A., Tucker, R., Jampani, V., Makadia, A., Snavely, N., and Kanazawa, A. Infinite nature: Perpetual view generation of natural scenes from a single image. In *Proceedings of the IEEE/CVF International Conference on Computer Vision (ICCV)*, October 2021.
- McCormac, J., Handa, A., Leutenegger, S., and Davison, A. J. Scenenet rgb-d: 5m photorealistic images of synthetic indoor trajectories with ground truth. *arxiv:1612.05079*, 2016.
- Meng, C., He, Y., Song, Y., Song, J., Wu, J., Zhu, J.-Y., and Ermon, S. Sdedit: Guided image synthesis and editing with stochastic differential equations. *arXiv:2108.01073*, 2021.
- Nichol, A. and Dhariwal, P. Improved denoising diffusion probabilistic models. *arXiv:2102.09672*, 2021.
- Nichol, A., Dhariwal, P., Ramesh, A., Shyam, P., Pamela Mishkin, B. M., Sutskever, I., and Chen, M. GLIDE: Towards Photorealistic Image Generation and Editing with Text-Guided Diffusion Models. *arXiv:2112.10741*, 2021.
- Nichol, A., Jun, H., Dhariwal, P., Mishkin, P., and Chen, M. Point-e: A system for generating 3d point clouds from complex prompts. *arXiv:2212.08751*, 2022.
- Ning, J., Li, C., Zhang, Z., Geng, Z., Dai, Q., He, K., and Hu, H. All in tokens: Unifying output space of visual tasks via soft token. *arXiv:2301.02229*, 2023.
- Poole, B., Jain, A., Barron, J. T., and Mildenhall, B. Dreamfusion: Text-to-3d using 2d diffusion. *arXiv:2209.14988*, 2022.
- Ramesh, A., Dhariwal, P., Nichol, A., Chu, C., and Chen, M. Hierarchical text-conditional image generation with clip latents. *arXiv:2204.06125*, 2022.
- Ranftl, R., Lasinger, K., Hafner, D., Schindler, K., and Koltun, V. Towards robust monocular depth estimation: Mixing datasets for zero-shot cross-dataset transfer. *arXiv:1907.0134*, 2019.
- Ranftl, R., Bochkovskiy, A., and Koltun, V. Vision transformers for dense prediction. In *International Conference on Computer Vision (ICCV)*, pp. 12179–12188, 2021.
- Ranzato, M., Chopra, S., Auli, M., and Zaremba, W. Sequence level training with recurrent neural networks. In *4th International Conference on Learning Representations (ICLR)*, 2016.
- Ren, Z. and Lee, Y. J. Cross-domain self-supervised multi-task feature learning using synthetic imagery. *arXiv:1711.09082*, 2017.
- Rockwell, C., Fouhey, D. F., and Johnson, J. Pixelsynth: Generating a 3d-consistent experience from a single image. *IEEE/CVF International Conference on Computer Vision (ICCV)*, 2021.
- Rombach, R., Blattmann, A., Lorenz, D., Esser, P., and Ommer, B. High-resolution image synthesis with latent diffusion models. In *Proceedings of the IEEE/CVF Conference on Computer Vision and Pattern Recognition*, pp. 10684–10695, 2022.
- Saharia, C., Chan, W., Chang, H., Lee, C. A., Ho, J., Salimans, T., Fleet, D. J., and Norouzi, M. Palette: Image-to-Image Diffusion Models. In *SIGGRAPH*, 2022a.
- Saharia, C., Chan, W., Saxena, S., Li, L., Whang, J., Denton, E., Ghasemipour, S. K. S., Ayan, B. K., Mahdavi, S. S., Lopes, R. G., Salimans, T., Ho, J., Fleet, D. J., and Norouzi, M. Photorealistic Text-to-Image Diffusion Models with Deep Language Understanding. In *NeurIPS*, 2022b.
- Saharia, C., Ho, J., Chan, W., Salimans, T., Fleet, D. J., and Norouzi, M. Image super-resolution via iterative refinement. *IEEE Trans. PAMI*, 2022c.
- Salimans, T. and Ho, J. Progressive distillation for fast sampling of diffusion models. *arXiv:2202.00512*, 2022.
- Savinov, N., Chung, J., Binkowski, M., Elsen, E., and van den Oord, A. Step-unrolled denoising autoencoders for text generation. In *International Conference on Learning Representations*, 2022. URL <https://openreview.net/forum?id=T0GpzBQ1Fg6>.

- Saxena, A., Chung, S., and Ng, A. Learning depth from single monocular images. In Weiss, Y., Schölkopf, B., and Platt, J. (eds.), *Advances in Neural Information Processing Systems*, volume 18. MIT Press, 2005.
- Saxena, A., Sun, M., and Ng, A. Y. Make3d: Learning 3d scene structure from a single still image. *IEEE Transactions on Pattern Analysis and Machine Intelligence*, 31(5):824–840, 2009.
- Silberman, N., Hoiem, D., Kohli, P., and Fergus, R. Indoor segmentation and support inference from rgb-d images. In *European Conference on Computer Vision (ECCV)*, pp. 746–760. Springer, 2012.
- Sohl-Dickstein, J., Weiss, E., Maheswaranathan, N., and Ganguli, S. Deep unsupervised learning using nonequilibrium thermodynamics. In *International Conference on Machine Learning*, pp. 2256–2265. PMLR, 2015.
- Song, Y., Sohl-Dickstein, J., Kingma, D. P., Kumar, A., Ermon, S., and Poole, B. Score-based generative modeling through stochastic differential equations. In *International Conference on Learning Representations*, 2021.
- Stommel, M., Beetz, M., and Xu, W. Inpainting of missing values in the kinect sensor’s depth maps based on background estimates. *IEEE Sensors Journal*, 14(4):1107–1116, 2014.
- Sun, P., Kretschmar, H., Dotiwalla, X., Chouard, A., Patnaik, V., Tsui, P., Guo, J., Zhou, Y., Chai, Y., Caine, B., Vasudevan, V., Han, W., Ngiam, J., Zhao, H., Timofeev, A., Ettinger, S., Krivokon, M., Gao, A., Joshi, A., Zhao, S., Cheng, S., Zhang, Y., Shlens, J., Chen, Z., and Anguelov, D. Scalability in perception for autonomous driving: Waymo open dataset. In *CVPR*, 2020.
- Tan, M. and Le, Q. Efficientnet: Rethinking model scaling for convolutional neural networks. In *International Conference on Machine Learning (ICML)*, pp. 6105–6114, 2019.
- Wang, S., Saharia, C., Montgomery, C., Pont-Tuset, J., Noy, S., Pellegrini, S., Onoe, Y., Laszlo, S., Fleet, D. J., Soricut, R., Baldridge, J., Norouzi, M., Anderson, P., and Chan, W. Imagen editor and editbench: Advancing and evaluating text-guided image inpainting. *arXiv:2212.06909*, 2022.
- Watson, D., Chan, W., Martin-Brualla, R., Ho, J., Tagliasacchi, A., and Norouzi, M. Novel view synthesis with diffusion models. *arXiv:2210.04628*, 2022.
- Williams, R. J. and Zipser, D. A learning algorithm for continually running fully recurrent neural networks. *Neural Computation*, 1(2):270–280, 1989. doi: 10.1162/neco.1989.1.2.270.
- Xie, Z., Geng, Z., Hu, J., Zhang, Z., Hu, H., and Cao, Y. Revealing the dark secrets of masked image modeling. *arxiv:2205.13543*, 2022.
- Xu, D., Alameda-Pineda, X., Ouyang, W., Ricci, E., Wang, X., and Sebe, N. Probabilistic graph attention network with conditional kernels for pixel-wise prediction. *Transactions on Pattern Analysis and Machine Intelligence (TPAMI)*, 2020.
- Yin, W., Liu, Y., Shen, C., and Yan, Y. Enforcing geometric constraints of virtual normal for depth prediction. In *International Conference on Computer Vision (ICCV)*, pp. 5684–5693, 2019.
- Yu, L., Zhang, W., Wang, J., and Yu, Y. Seqgan: Sequence generative adversarial nets with policy gradient. *arXiv:1609.05473*, 2016.
- Zhang, R., Isola, P., and Efros, A. A. Colorful image colorization. *arXiv:1603.08511*, 2016.
- Zhao, J., Yan, K., Zhao, Y., Guo, X., Huang, F., and Li, J. Transformer-based dual relation graph for multi-label image recognition. In *International Conference on Computer Vision (ICCV)*, pp. 163–172, 2021.
- Zhou, B., Lapedriza, A., Khosla, A., Oliva, A., and Torralba, A. Places: A 10 million image database for scene recognition. *IEEE Transactions on Pattern Analysis and Machine Intelligence*, 2017.
- Zhou, B., Krähenbühl, P., and Koltun, V. Does computer vision matter for action? *arXiv:1905.12887*, 2019.

## A. Additional results

Table 6. Detailed ablation for handling incomplete depth on the NYU depth v2 dataset.

|                   | $\delta_1 \uparrow$ | $\delta_2 \uparrow$ | $\delta_3 \uparrow$ | REL $\downarrow$ | RMS $\downarrow$ | $\log_{10} \downarrow$ |
|-------------------|---------------------|---------------------|---------------------|------------------|------------------|------------------------|
| Baseline          | 0.939               | 0.985               | 0.994               | 0.079            | 0.336            | 0.034                  |
| SUD only          | 0.944               | 0.986               | 0.995               | 0.076            | 0.325            | 0.033                  |
| Infilling only    | 0.940               | 0.985               | 0.995               | 0.077            | 0.338            | 0.034                  |
| SUD and infilling | 0.944               | 0.986               | 0.995               | 0.075            | 0.324            | 0.032                  |

Table 7. Detailed ablation for handling incomplete depth on the KITTI dataset.

|                   | $\delta_1 \uparrow$ | $\delta_2 \uparrow$ | $\delta_3 \uparrow$ | REL $\downarrow$ | Sq-rel $\downarrow$ | RMS $\downarrow$ | RMS log $\downarrow$ |
|-------------------|---------------------|---------------------|---------------------|------------------|---------------------|------------------|----------------------|
| Baseline          | 0.920               | 0.985               | 0.996               | 0.115            | 0.550               | 3.563            | 0.142                |
| SUD only          | 0.938               | 0.986               | 0.996               | 0.075            | 0.468               | 3.437            | 0.117                |
| Infilling only    | 0.949               | 0.990               | 0.997               | 0.066            | 0.408               | 3.187            | 0.106                |
| SUD and infilling | 0.951               | 0.991               | 0.997               | 0.064            | 0.389               | 3.104            | 0.103                |

Table 8. Detailed ablation for pretraining on the NYU depth v2 dataset.

|   | $\delta_1 \uparrow$ | $\delta_2 \uparrow$ | $\delta_3 \uparrow$ | REL $\downarrow$ | RMS $\downarrow$ | $\log_{10} \downarrow$ |       |
|---|---------------------|---------------------|---------------------|------------------|------------------|------------------------|-------|
| From scratch                            |                     | 0.777               | 0.920               | 0.969            | 0.155            | 0.601                  | 0.069 |
| Unsupervised pretraining only           |                     | 0.877               | 0.964               | 0.988            | 0.116            | 0.450                  | 0.049 |
| Supervised pretraining only             |                     | 0.936               | 0.980               | 0.992            | 0.081            | 0.352                  | 0.035 |
| Unsupervised and supervised pretraining |                     | 0.944               | 0.986               | 0.995            | 0.075            | 0.324                  | 0.032 |

Table 9. Detailed ablation for pretraining on the KITTI dataset.

|   | $\delta_1 \uparrow$ | $\delta_2 \uparrow$ | $\delta_3 \uparrow$ | REL $\downarrow$ | Sq-rel $\downarrow$ | RMS $\downarrow$ | RMS log $\downarrow$ |
|---|---------------------|---------------------|---------------------|------------------|---------------------|------------------|----------------------|
| From scratch                            | 0.880               | 0.959               | 0.986               | 0.103            | 0.801               | 4.643            | 0.172                |
| Unsupervised pretraining only           | 0.912               | 0.978               | 0.993               | 0.086            | 0.604               | 3.901            | 0.137                |
| Supervised pretraining only             | 0.936               | 0.985               | 0.996               | 0.075            | 0.470               | 3.448            | 0.118                |
| Unsupervised and supervised pretraining | 0.951               | 0.991               | 0.997               | 0.064            | 0.389               | 3.104            | 0.103                |

Table 10. Detailed ablation for the choice of loss function on the NYU depth v2 dataset.

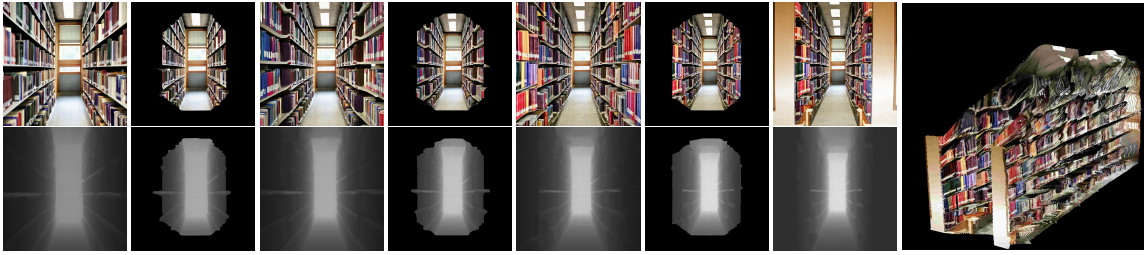
|       | $\delta_1 \uparrow$ | $\delta_2 \uparrow$ | $\delta_3 \uparrow$ | REL $\downarrow$ | RMS $\downarrow$ | $\log_{10} \downarrow$ |
|-------|---------------------|---------------------|---------------------|------------------|------------------|------------------------|
| $L_2$ | 0.932               | 0.981               | 0.994               | 0.085            | 0.349            | 0.037                  |
| $L_1$ | 0.944               | 0.986               | 0.995               | 0.075            | 0.324            | 0.032                  |

Table 11. Detailed ablation for the choice of loss function on the KITTI dataset.

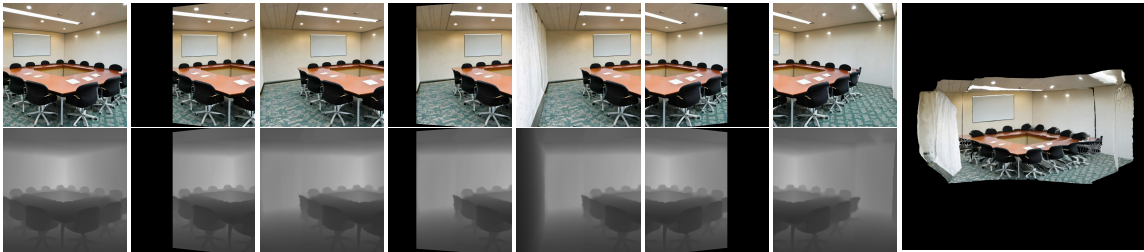
|       | $\delta_1 \uparrow$ | $\delta_2 \uparrow$ | $\delta_3 \uparrow$ | REL $\downarrow$ | Sq-rel $\downarrow$ | RMS $\downarrow$ | RMS log $\downarrow$ |
|-------|---------------------|---------------------|---------------------|------------------|---------------------|------------------|----------------------|
| $L_2$ | 0.943               | 0.990               | 0.997               | 0.071            | 0.416               | 3.221            | 0.110                |
| $L_1$ | 0.951               | 0.991               | 0.997               | 0.064            | 0.389               | 3.104            | 0.103                |

Monocular Depth Estimation using Diffusion Models

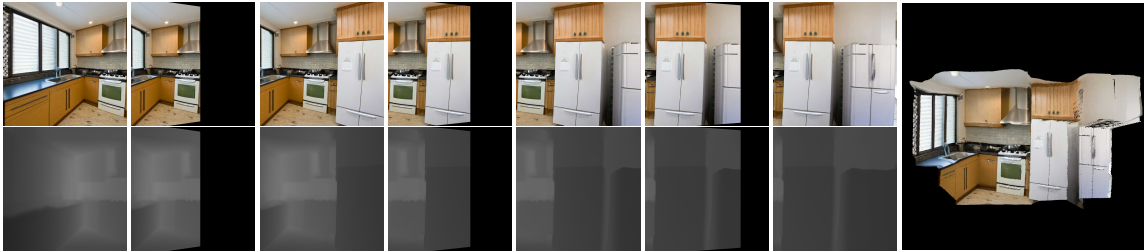
---



Prompt: A library.



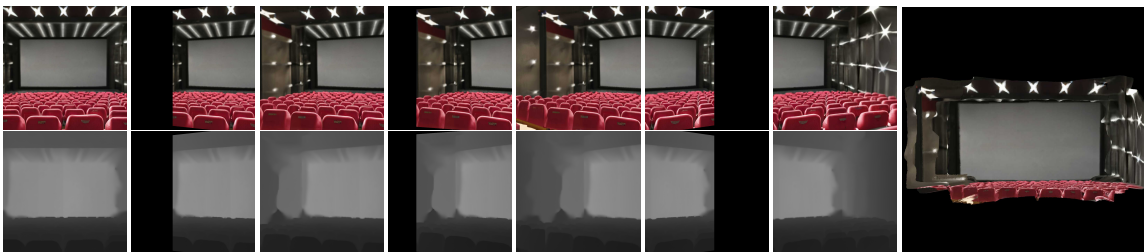
Prompt: A meeting room.



Prompt: A kitchen.

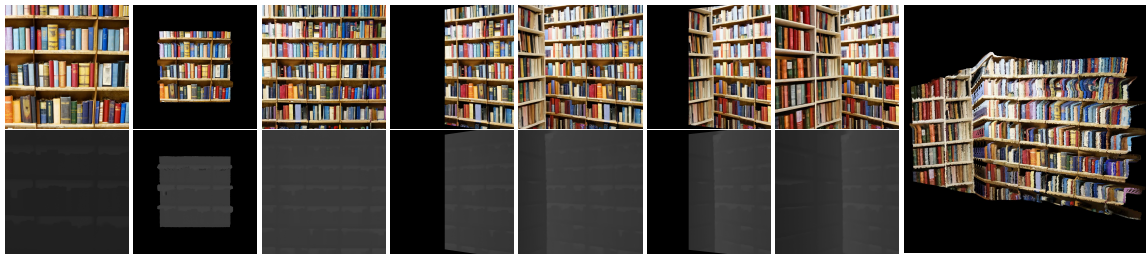


Prompt: A warehouse.



Prompt: A movie theatre.

## Monocular Depth Estimation using Diffusion Models



Prompt: A bookstore.

Figure 6. Text to 3D samples. Given a text prompt, an image is first generated using Imagen (first row of first column), after which depth is estimated (second row of first column). Subsequently the camera is moved to reveal new parts of the scene which are infilled using an image completion model and DepthGen (which conditions on both the incomplete depth map and the filled image). At each step, newly generated RGBD points are added to a global point cloud which is visualized in the rightmost column.

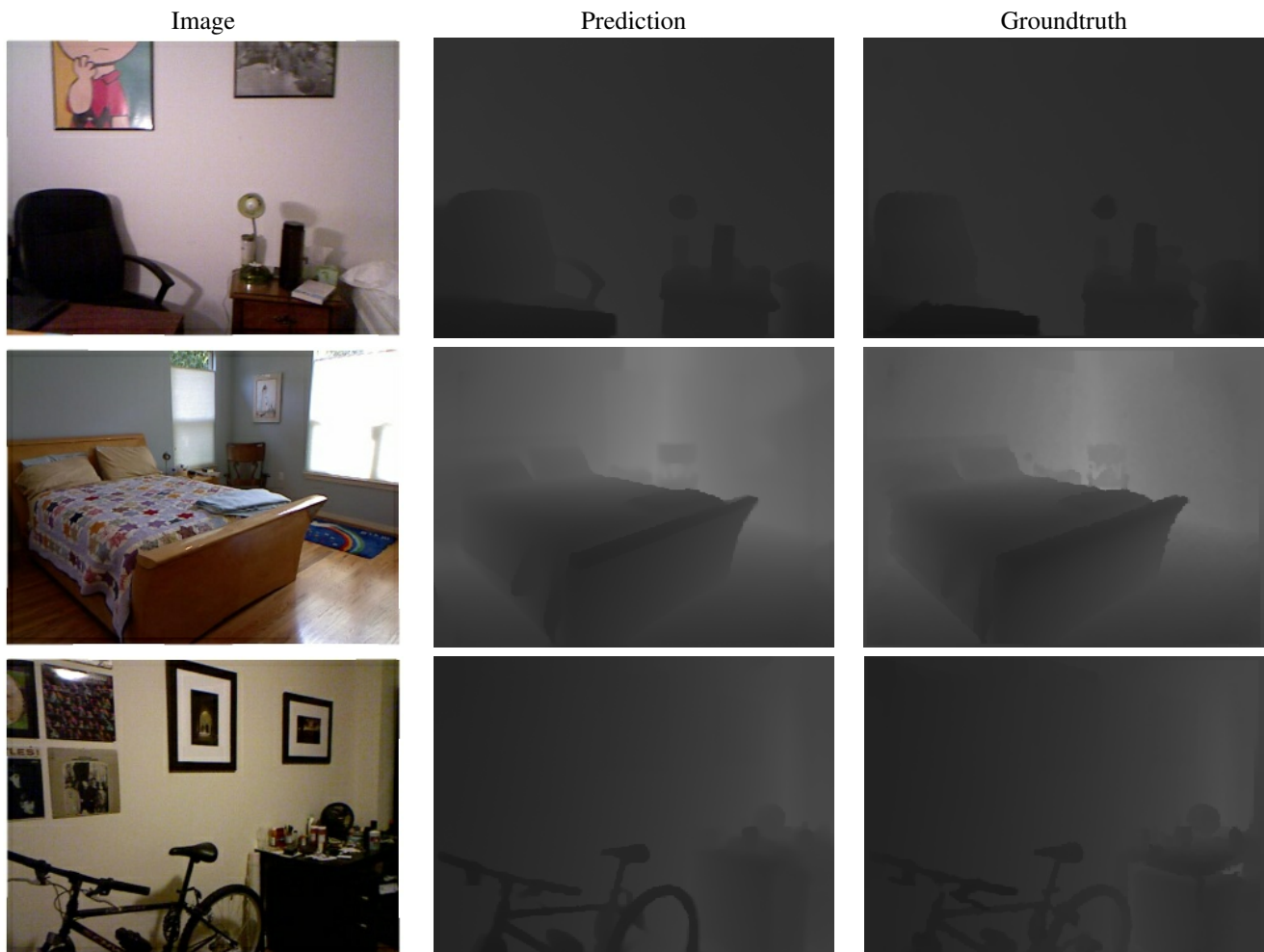


Figure 7. Predictions on the NYU Depth V2 val dataset.



Figure 8. Predictions on the KITTI val dataset. Note that we extract the sky region using a sky segmenter and fix the sky depth to the max depth during inference using replacement guidance.

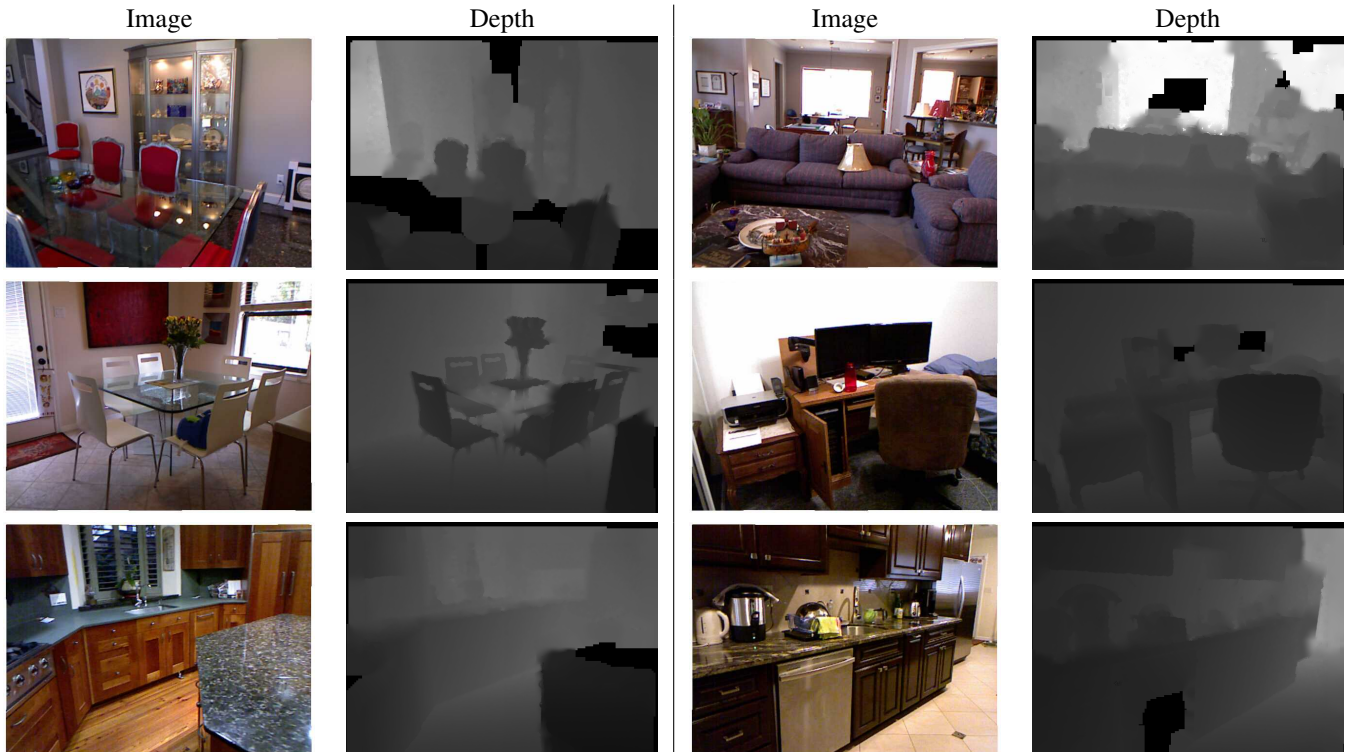


Figure 9. Examples of RGB images and their corresponding depth maps from the NYU depth v2 training set containing missing depth.